

RESEARCH ARTICLE | JULY 15 2025

Electron cyclotron emission measurements and modeling in optically semi-transparent plasma on the HSX stellarator

G. M. Weir   ; L. Singh  ; K. M. Likin; N. B. Marushchenko  ; Y. Turkin 



Rev. Sci. Instrum. 96, 073503 (2025)

<https://doi.org/10.1063/5.0257903>



Articles You May Be Interested In

Electron cyclotron current drive simulations for finite collisionality plasmas in Wendelstein 7-X using the full linearized collision model

Phys. Plasmas (November 2016)

A deterministic thermostat for controlling temperature using all degrees of freedom

J. Chem. Phys. (February 2014)

Preparatory study of feasibility for a vertical viewing electron cyclotron emission diagnostic for the JT-60SA tokamak

Rev. Sci. Instrum. (August 2024)

17 July 2025 16:29:12



Review of
Scientific Instruments
Special Topics Now Online

[Learn More](#)

Electron cyclotron emission measurements and modeling in optically semi-transparent plasma on the HSX stellarator

Cite as: Rev. Sci. Instrum. 96, 073503 (2025); doi: 10.1063/5.0257903

Submitted: 13 January 2025 • Accepted: 14 May 2025 •

Published Online: 15 July 2025



View Online



Export Citation



CrossMark

G. M. Weir,^{1,2,a)}  L. Singh,²  K. M. Likin,²  N. B. Marushchenko,¹  and Y. Turkin¹ 

AFFILIATIONS

¹Max Planck Institute for Plasma Physics, EURATOM Association, Wendelsteinstr. 1, 17491 Greifswald, Germany

²HSX Plasma Laboratory, University of Wisconsin-Madison, Madison, Wisconsin 53706, USA

^{a)}Author to whom correspondence should be addressed: gavin.weir@ipp.mpg.de

ABSTRACT

On the Helically Symmetric Experiment (HSX), electron cyclotron emission (ECE) at the second harmonic of the electron gyrofrequency is measured with a 16-channel heterodyne receiver. An ECE radiometer diagnostic has been calibrated with a broadband frequency source, allowing independent measurements of the electron temperature. The antenna pattern has a significant impact on the measurements, and modeling its effect is necessary to produce an ECE radiation temperature spectrum. Measurements, calibration results, and modeling of the ECE data are presented in this paper. At a relatively high plasma density, HSX plasmas are thermal, and the radiation temperature measured by the radiometer is in good agreement with the electron temperature measured by a Thomson scattering diagnostic. At a relatively low plasma density, the deviation from a Maxwellian distribution is large, and asymmetry in the radiation temperature profile is measured. These measurements are supported by single-pass and multi-pass ray tracing calculations of the electron cyclotron emission using the TRAVIS ray tracing code. Thermal and nonthermal electron populations exist in HSX, and the effect of these populations on the asymmetry in the measured emission is presented.

Published under an exclusive license by AIP Publishing. <https://doi.org/10.1063/5.0257903>

I. INTRODUCTION

Electron Cyclotron Emission (ECE) is used as a spatially and temporally resolved electron temperature diagnostic in magnetically confined plasma experiments.¹ Radiation transport modeling is necessary for the design and use of ECE diagnostics, especially for emission that does not reach the blackbody level or for radiometers that operate near the cutoff frequency for the observed plasma wave, where refraction can alter the measurement position. The latter situation commonly arises in the pedestal region of H-mode plasmas in tokamaks,² as well as in overdense plasmas like those produced on the Wendelstein 7-X (W7-X) experiment.^{3,4} W7-X operates at plasma densities in excess of 10^{20} m^{-3} , where wave refraction may significantly modify the interpretation of the ECE measurements.^{5,6} The Helically Symmetric Experiment (HSX) is a stellarator with an approximately quasi-helical magnetic field^{7,8} that produces plasmas with Electron Cyclotron Resonance Heating (ECRH) with a maximum on-axis magnetic field strength of 1.0 T. The maximum

achievable plasma density is limited to $\sim 6 \times 10^{18} \text{ m}^{-3}$ by wave refraction,⁹ and the plasma is optically semi-transparent to the emission of the extraordinary wave at the second harmonic of the electron gyrofrequency (X2).

An additional consideration for modeling the electron cyclotron emission in ECRH driven plasmas is the deviation of the electron distribution from a Maxwellian. In experiments with ECRH, it is possible to develop nonthermal electron distributions when the absorbed ECRH power density, p_{abs} , is high and the condition of small disturbance, $p_{abs}/n_e T_e \nu_e \ll 1$, is broken for a population of directly heated electrons. Here, ν_e is the collision frequency of the resonant electrons. In this case, collisional relaxation is insufficient to thermalize the electrons, and the deviation from a Maxwellian distribution function can be large.¹⁰ The balance of emission and reabsorption along the line-of-sight of an ECE diagnostic determines the shape and magnitude of the measured electron cyclotron emission spectrum, and the measured spectrum can be modeled through the solution of the radiation transfer equation.¹¹

The local cyclotron emission and reabsorption are determined by integrals over the electron distribution function and its derivatives in velocity space, and consequently, nonthermal electrons may produce a significant contribution to the resulting electron cyclotron spectrum.¹²

The ECE diagnostic on HSX is an absolutely calibrated, 16-channel heterodyne radiometer. A calibration source within the experimental vacuum vessel, such as the *in situ* calibration unit planned for the ITER tokamak¹³ or that installed on the J-Text tokamak,¹⁴ is not feasible on HSX due to material and spatial constraints. The antenna pattern of the ECE diagnostic on HSX and the plasma parameters have a significant impact on the measured radiation temperature spectrum, $T_r(\omega)$, and modeling of the emission sampled by the diagnostic is necessary to accurately determine the electron temperature profile, $T_e(r/a)$.

In HSX, the ECRH power densities are comparable to those measured on larger and denser fusion experiments ($>1 \text{ MW/m}^3$).⁹ Previous experiments on HSX with 28 GHz extraordinary wave heating at the second harmonic of the electron gyrofrequency showed that a nonthermal component exists with 50 kW of launched ECRH power. Under these conditions, a bi-Maxwellian distribution function model with a 5 keV tail reproduced the asymmetry in the radiation temperatures between the low and high magnetic field sides of the magnetic-axis that were measured using an eight-channel ECE radiometer.¹⁵ In addition, tail populations with energies up to 12 keV have been observed to drive energetic electron instabilities.¹⁶

At a relatively low plasma density and high heating power, a nonthermal component also exists in HSX with 28 GHz ordinary wave heating at the first harmonic of the electron gyrofrequency. In this case, asymmetry is measured in the radiation temperatures with 85 kW of launched heating power below line-average plasma densities of $3.5 \times 10^{18} \text{ m}^{-3}$ using the 16-channel system. The 5D Fokker-Planck code GNET¹⁷ has been used to model spontaneous parallel flows that develop in HSX due to the ECRH driven flux. At high ECRH power-per-particle, a significant nonthermal distribution can develop in HSX that is associated with higher plasma flows.¹⁸ At higher plasma density and lower ECRH power-per-particle, the radiation temperature is in agreement with the electron temperature measured with a ten-channel Thomson scattering diagnostic.¹⁹

The ECE radiometer is described in Sec. II, and its absolute calibration is described in Sec. II A. Simplified 1D and 2D models are used to estimate the optical depth of the measured emission, and these results are compared to a 3D ray tracing code in Sec. II B. An iterative procedure is necessary to convert the measured radiation temperature spectrum to an electron temperature profile, and the results from a multi-pass emission model are presented in Sec. II C. The localization of the emission is discussed in Sec. II D. Finally, asymmetry in the radiation temperature profile is discussed in Sec. III, where bi-Maxwellian modeling of the ECE emission is invoked to explain the ECE spectrum in high power density HSX discharges.

II. THE HSX RADIOMETER, ITS CALIBRATION, AND MODELING

The radiometer used for this study on HSX is a single sideband receiver that measures electron cyclotron emission from plasma

heated by ECRH at 28 GHz, corresponding to the fundamental or second harmonic of the electron gyrofrequency. Its pyramidal horn antenna acquires emission perpendicular to the main magnetic field from the extraordinary wave. For a main magnetic field strength of 0.5 T, the electron cyclotron emission originating from the plasma core is between 22 and 34 GHz, while for a main magnetic field strength of 1.0 T, the emission is between 50 and 63 GHz. With a mixer diode unit and a 42.5 GHz local oscillator, the high frequency bands are down-converted to intermediate frequencies (IFs) between 8 and 19 GHz. After two stages of amplification, the signal is divided into 16 channels with IF bandwidths of either 200 or 400 MHz to spatially separate the plasma emission. The IF filters can be exchanged as necessary for particular experiments with repeated absolute calibration. Each IF channel is connected to a low noise crystal detector followed by a 250 kHz video amplifier prior to digitization. A 28 GHz notch filter protects the receiver from unabsorbed ECRH power during 0.5 T machine operation, while the notch filter is replaced by a high-pass waveguide filter for operation at 1.0 T. To increase the spatial resolution, a focusing mirror is placed in front of the horn antenna as close as possible to the plasma. A rectangular Ka-band (WR-28) waveguide channels the microwave power from the antenna to the detection unit, and a thin polyimide film brazed into the waveguide serves as a vacuum barrier window.

A. Absolute calibration of the radiometer

To measure the sensitivity of the heterodyne receiver, including losses along the waveguide transmission line, a noise source is connected to the waveguide next to the vacuum barrier window. The Excess Noise Ratio (ENR) of the Quinstar (QNS-FB15LV) noise source is $(17 \pm 0.8) \text{ dB}$ in the 50–75 GHz frequency range. An analog lock-in amplifier is used to measure the response of the receiver to the output from the noise source while it is operated with a 50% duty cycle, and the Y-factor method is used to determine the power

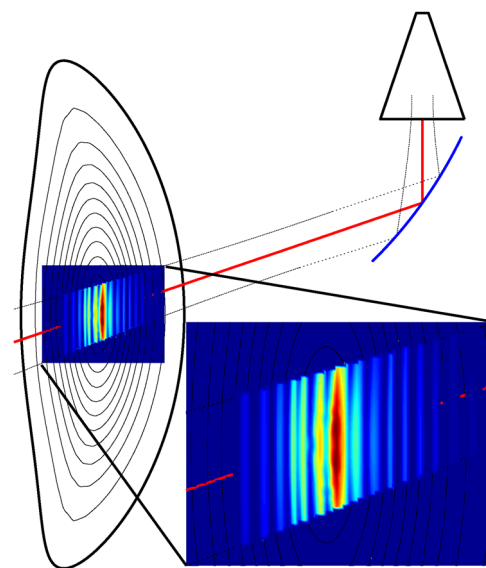


FIG. 1. Warm-plasma resonance for each ECE channel in the helical cut of HSX (vertical is normal to the helical direction).

gain (G in Watts/Volt) for each channel of the receiver. The measured sensitivity of the HSX radiometer is stable while the receiver and waveguide remain unchanged from their calibration positions.

The voltage response of each channel, V_r , is related to the radiation temperature, $T_r(\omega)$ in eV, through $BT_r \approx \frac{2\pi\lambda^2}{\Omega A_e} GV_r$. Here, λ is the wavelength in meters, and B is the IF bandwidth of each channel in hertz. The étendue of the emission is the product of the solid angle of the emission subtended by the antenna, Ω in steradians, and the aperture efficiency of the antenna, A_e in square meters. It should be noted that modeling is necessary to determine the étendue for the most central channels of the ECE diagnostic ($r/a < 0.2$), where the magnetic flux surfaces are smaller than the E-plane Gaussian beam width of the antenna, as illustrated in Fig. 1. The coupling between the wave beam and the transmission line is estimated as 0.88. Truncation losses on the mirror are negligible ($< 0.3\%$), and a polyimide film similar to the vacuum barrier window is used as a DC break during absolute calibration.

B. Resonance modeling

The resonance location and width, including the power distribution of the antenna pattern and warm plasma effects, are determined by calculating the emission for each ECE channel. The cold plasma resonance location is calculated from the intersection of the quasi-optical beam with the resonant magnetic field, which may be determined from either a look-up table or from a pre-calculated VMEC²⁰ equilibrium file, including the bandwidth of each channel. The emission is then calculated either using an analytic model for the absorption coefficient²¹ or by the ray tracing code TRAVIS.^{22,23}

In the cylindrical coordinate system of HSX, the helical cut of the plasma is defined perpendicular to the magnetic axis, which at the ECE antenna position is pitched 28.8° with respect to the vertical direction. The warm-plasma resonance in this helical cut, including the bandwidth of each channel, the power distribution of the Gaussian beam, and the finite electron temperature and plasma density within the region sampled by each ECE channel, is shown for a representative plasma discharge in Fig. 1. The optical depth is the integrated absorption along the view of the diagnostic, and it is used as a dimensionless measure of the emission intensity according to Kirchhoff's law.¹¹ For an optical depth greater than ~ 2 , the emission approaches the blackbody level, and the radiation intensity is proportional to the electron temperature.

The optical depth from a 1D absorption calculation along the ECE beam-axis, $\tau_\omega = \int \alpha_\omega ds$, and the 2D absorption calculation in the helical cut of HSX, $\tau_\omega = \frac{1}{\delta Z} \iint \alpha_\omega dRdZ$, where δZ is the beam width at the resonance location, are shown in Fig. 2. The optical depth calculated in the full 3D magnetic geometry of HSX using the ray tracing code TRAVIS is also shown in Fig. 2. These calculations used the electron temperature and plasma density measured through Thomson scattering. For the ray tracing calculation shown in Fig. 2, the ECE wave pattern was modeled using a Gaussian intensity distribution with a beam half-width of 2 cm, an infinite focal length, and 40 rays distributed between 5 concentric rings about the central ray.

The 1D absorption calculation overestimates the optical depth in the core of the plasma because it passes through the peak in the emission intensity. The 2D absorption calculation encapsulates 90% of the power of the ECE beam, and the sampling volume is weighted

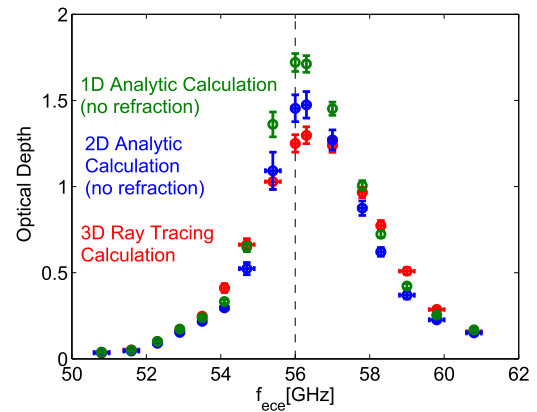


FIG. 2. Optical depth from 1D and 2D analytic calculations and optical depth from 3D ray tracing, which includes refraction, in the real geometry of HSX.

by the power density of the quasi-optical beam.²⁴ However, the 2D calculation also overestimates the absorption in the core of the plasma because the ECE beam width is greater than the dimension of the sampled flux surfaces.

The antenna gathers emission from above the plasma midplane, and the viewing geometry is not perfectly perpendicular to the magnetic flux surfaces. Consequently, there is a finite asymmetry in the density gradient sampled by the quasi-optical beam across its perpendicular axis, and this can lead to asymmetric beam-broadening due to the refraction of the beam edges. These refraction effects are modeled via ray tracing as in Ref. 9. The maximum core density of HSX during 1 T operation is $\sim 35\%$ of the X2 cutoff density ($2 \times 10^{19} \text{ m}^{-3}$), and wave refraction does not have a significant impact on the radiation transport for the ECE diagnostic on HSX.

C. Emission modeling

Despite the power density weighting, the 2D analytic calculation overestimates the étendue of the plasma subtended by the ECE antenna, and this contributes to the overestimate in the absorption in the core. The Gaussian beam width of the ECE antenna at the resonance is sufficient in regions of the plasma where the resonance is larger than the beam width. In the plasma core, the emitting volume is smaller than the ECE beam width, and this significantly impacts the radiation temperature measured by the diagnostic within $r/a < 0.2$. The overestimated absorption in this region leads to an underestimate in the electron temperature, and an iterative procedure is necessary to self-consistently determine the electron temperature in this region.

First, the absorption is calculated in the 2D helical cut of the antenna using an experimentally measured plasma density profile and an arbitrary initial electron temperature profile. Then, a synthetic radiation spectrum is calculated using the modeled profiles, and the result is compared to the measured spectrum. For the innermost channels, $r/a < 0.2$, the étendue is calculated from the full width at half max of the absorption shapes in the E-plane of the antenna during each iteration. This procedure is iterated until the model electron temperature profile and the absorption calculation are self-consistent with the measured radiation temperature. The

electron temperature is considered self-consistent when the difference between electron temperature iterations is less than 5 eV. The result of this iterative procedure is insensitive to the initial guess for the electron temperature profile. In the absence of wave refraction, this linear 2D iterative solution is sufficient in HSX. The emission from the high magnetic -field side is used to minimize the effect of nonthermal populations (Sec. III B) and relativistically down-shifted emission (Sec. II D) in the calculation of the electron temperature from the ECE radiation temperature. Both of these effects modify the emission from the low-field side of the magnetic axis and contribute to the asymmetry measured in the ECE radiation temperature that is discussed in Sec. III.

Although the calculated optical depth is below 2, the measured spectrum is significantly larger than that predicted from the solution of the radiation transfer equation for a single-pass through the plasma along the diagnostic line-of-sight, $T_r^{synth}(\omega) = \int T_e(s)\alpha_\omega(s) \exp[-\tau_\omega(s)]ds$. Consequently, a multi-pass radiation transfer model is necessary to match the experimentally measured spectrum, $T_r(\omega) = T_r^{synth}(\omega)/(1 - \rho \exp[-\tau_\omega])$. Here, ρ is the effective reflection coefficient of the vacuum vessel wall.

In the limit of unity wall reflectivity, $\rho = 1$, the radiation temperature is equal to the blackbody electron temperature through multiple reflections near the maximum achievable plasma density in HSX. The electron temperature profile (T_e^{ECE}) determined from the ECE radiation temperature measured on the high-field side of the magnetic axis (T_{rad}^{ECE}) is compared to the electron temperature measured by Thomson scattering (T_e^{TS}) in Fig. 3. In this case, the radiation temperature is equivalent to the blackbody electron temperature in HSX, and the effective reflectivity is approximately unity.^{25,26} The effective minor radius of the ECE resonance is taken as the center-of-mass of the emission profile for each channel. The horizontal error bars in Fig. 3 are meant to represent the natural linewidth of the emission, although there is a small contribution from changes in the magnetic field strength between plasma discharges.

The iterative procedure described here can alter transient behavior, and caution should be applied for experiments that require

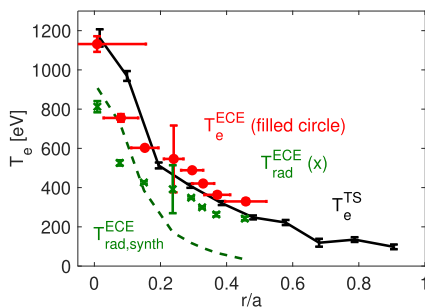


FIG. 3. Absolutely calibrated ECE radiation temperature measured on the high-field side of the magnetic axis (green-x's), analytic first-pass ECE radiation temperature estimate (green dashed line), inverted ECE electron temperature profile calculated using the iterative procedure described in the text (red filled circles), and Thomson scattering measurements of the electron temperature profile (black solid line) in plasma produced with 85 kW launched ECRH power at $n_e = 4 \times 10^{18} \text{ m}^{-3}$ line-average plasma density.

high temporal resolution, such as the absorption measurement discussed in Sec. II D, or the heat pulse propagation experiments on HSX, which are separately reported.²⁷ To avoid altering the temporal behavior of the ECE electron temperature, the iterative calculation was applied to the average electron radiation temperature, and the results were applied uniformly to determine the electron temperature during these experiments.

D. Localization of the emission

The high effective wall reflectivity of HSX can lead to a loss of spatial resolution as the emission undergoes multiple passes through the plasma. To investigate this effect, the emission localization is calculated using both a single-pass and a multi-pass ray tracing model implemented in the TRAVIS code. The emission, including the effect of reabsorption, is calculated with up to 3 passes through the plasma that are reflected by the vacuum vessel. This model has previously been applied successfully in the context of multi-pass ECRH absorption in HSX.⁹

Along a perpendicular line-of-sight, the ECE intensity from the low-field side (LFS) region of the plasma exceeds that from the high-field side (HFS) of the magnetic axis with the same effective plasma radius, because the LFS and HFS channels acquire regions with different electron temperature and plasma density due to relativistic broadening of the emission. In optically semi-transparent plasma, the asymmetry in the ECE spectrum measured across the magnetic axis is primarily due to the decreased efficiency of reabsorption along the line-of-sight of the diagnostic for emission originating on the LFS of the device. This results in a loss of localization for channels with cold plasma resonance on the LFS of the magnetic axis. This is illustrated in Fig. 4, where single-pass ray tracing calculations are used to model emission sampled by two channels from two experiments on HSX.

The emission, determined from the emissivity accounting for reabsorption, is shown normalized to its peak value for channels with cold plasma resonances at $r/a = 0.15$ and $r/a = 0.5$ on both sides of the magnetic axis in Fig. 4. In the first case shown, the line-average plasma density is $n_e = 4 \times 10^{18} \text{ m}^{-3}$, as for the data shown in Fig. 3. In this case, the HFS emission approaches the blackbody level and matches Thomson scattering measurements of the electron temperature. In the second case, the line-average plasma density is $n_e = 2.5 \times 10^{18} \text{ m}^{-3}$, and the emission is optically semi-transparent. The two experimental cases discussed here are near the extrema in the experimental scan shown in Fig. 8, and these results are further discussed in Sec. III B.

In both experimental cases shown in Fig. 4(a), the single-pass ray tracing model predicts that the core channels have approximately symmetric normalized line shapes across the magnetic axis. There is a small asymmetry due to relativistically down-shifted emission into the LFS channel in the relatively high density case (solid lines in Fig. 4), and this asymmetry increases in the relatively low plasma density case (dashed-dotted lines in Fig. 4) as the contribution from core electrons increases.

There is a significant change in the asymmetry in the normalized emission shapes for the channels near the half-radius, which are shown in Fig. 4(b). In the relatively high plasma density case, the peaks in the normalized emission shapes are symmetric across the magnetic axis, but there is a comparable contribution to the LFS

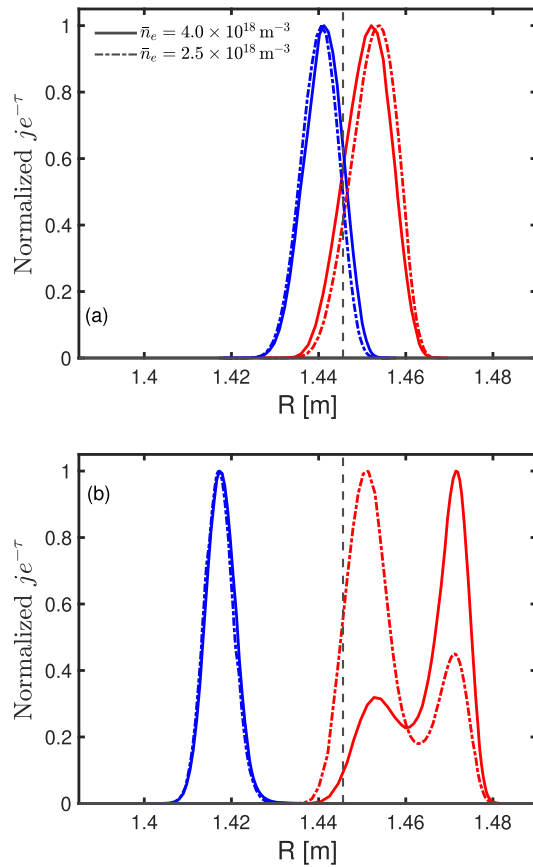


FIG. 4. Normalized single-pass emissivity accounting for reabsorption for relatively low ($n_e = 2.5 \times 10^{18} \text{ m}^{-3}$, dotted-dashed) and relatively high ($n_e = 4.0 \times 10^{18} \text{ m}^{-3}$, solid lines) plasma density. The emission from the high-field side (blue) and low-field side (red) of the magnetic axis is shown at both densities, and the magnetic axis is indicated by a vertical dashed line. The HFS channels approach the blackbody level in the relatively high density case, and the single-pass emission remains localized in both cases. The LFS channels sample relatively downshifted emission from the core of the plasma in both cases. (a) $r/a \approx 0.15$. (b) $r/a \approx 0.5$.

channel from core down-shifted emission. This is apparent for the first-pass emission shown in Fig. 5, where there is an asymmetry in the magnitude of the emission between the HFS and LFS of the magnetic axis, with a significant component of the first-pass emission from the LFS channel coming from the core.

In the relatively low plasma density case shown in Fig. 4(b), the peak in the normalized emission shape from the HFS channel is coincident with the higher density case. However, the peak in the normalized emission shape from the LFS channel shifts to the plasma core. In this case, the downshifted thermal emission from the core of the plasma dominates the LFS channel.

In the single-pass ray tracing model on HSX, the LFS channels outside of $\sim 20\%$ of the effective minor radius are not local measurements, with most of their emission originating from the plasma core, $r/a < 0.2$. The emission from the HFS and core channels remains localized near their cold plasma resonances in this

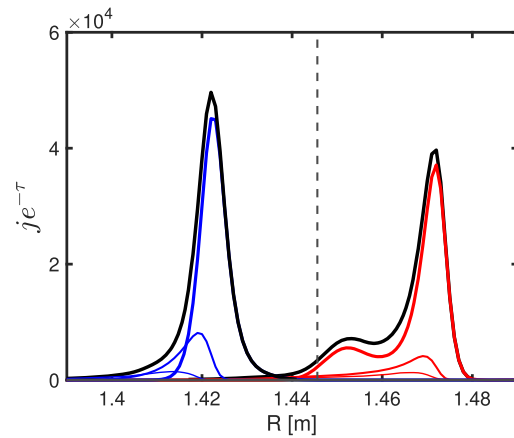


FIG. 5. Emissivity accounting for reabsorption considering three passes of radiation for high-field side (blue) and low-field side (red) channels near the mid-radius. The sum over passes is plotted in black. Colored linewidth decreases with the number of passes. The HFS channel remains localized near the cold plasma resonance after three passes of radiation through the plasma, while the LFS channel acquires additional core emission over multiple passes through the plasma.

single-pass model. The effect of multiple passes on the emission shapes is shown for channels with cold plasma resonances at $r/a = 0.5$ on both sides of the magnetic axis in Fig. 5. These calculations were performed for the relatively high plasma density case of Fig. 4, corresponding to the experimental profile shown in Fig. 3. For both channels, the first pass emission has its peak localized near the cold plasma resonances, although the LFS channel has a significant contribution of downshifted core emission. The magnitude of the second pass emission is significantly smaller than the first pass emission. The magnitude of the peak in the third pass emission is smaller than the second pass emission and negligible in comparison to the first pass emission. For the HFS channel, the second pass emission reinforces the first pass emission and does not significantly alter the localization of the channel. For the LFS channel, the effect of multiple reflections is to increase the relative contribution from hot, core electrons and thereby decrease the localization of the channel.

This multi-pass ray tracing model is consistent with previous measurements of the ECRH damping on HSX using an absolutely calibrated array of microwave diodes, which indicated a high degree of toroidal localization.²⁵ The total ECRH absorption has also been measured and was consistent with this multi-pass ray tracing model.⁹ The ECRH absorption profile can be measured using the difference in energy balance during ECRH turn-off, $\frac{dP}{dV} = \frac{3}{2} n_e \frac{dT_e}{dt} |_{t+} - |_{t-}$. Here, the electron temperature is measured by the absolutely calibrated ECE radiometer, and the plasma density profile is measured via Thomson scattering, and it is assumed constant over the 50 μs time-window after ECRH turn-off. This analysis was performed for a set of plasma discharges with modulated heating power during a transient transport experiment, and the IF filters of all 16 channels of the ECE radiometer were chosen to correspond to the region $r/a < 0.5$ to increase the spatial resolution in the plasma core. Time-traces of the ensemble average ECE electron temperature during ECRH turn-off for these discharges are shown in Fig. 6.

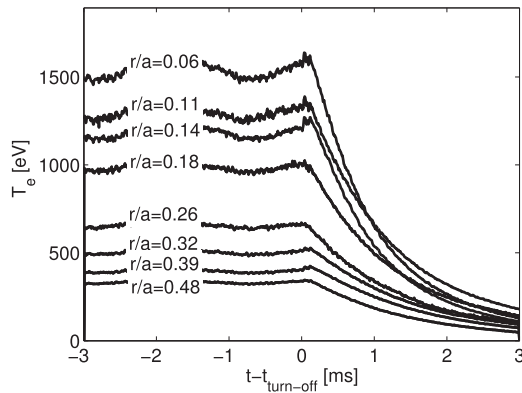


FIG. 6. ECE time-traces measured at ECRH turn-off during a modulated heating experiment (85 kW launched ECRH power, $n_e = 4 \times 10^{18} \text{ m}^{-3}$, 500 Hz modulation).

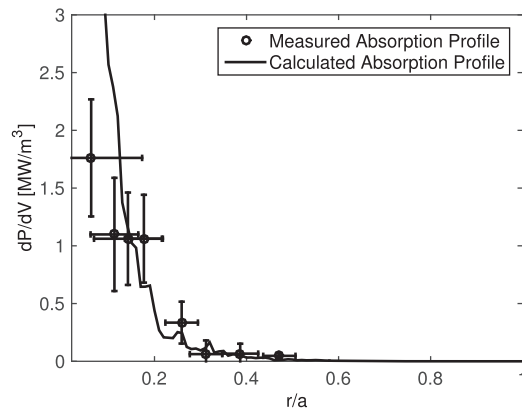


FIG. 7. ECRH absorption profile measured using the change in high-field side ECE after ECRH turn-off is compared to a multi-pass ray tracing model.

The resulting absorbed power profile is shown in Fig. 7, where it is compared to the ECRH power deposition profile calculated using the same multi-pass ray tracing model.⁹ The analysis is performed on each shot individually before the results are averaged. The multi-pass ray tracing calculation that is shown in Fig. 7 indicates that the ECRH absorption is localized to the core, which is consistent with the experimental measurement. The horizontal error bar is the natural linewidth from a single-pass emission model, as in Fig. 3, and the agreement with ray tracing indicates that the emission is highly localized between 10% and 50% of the effective minor radius, $0.1 < r/a < 0.5$. Measurements are not available outside of a 50% effective minor radius for these discharges.

III. NONTHERMAL ELECTRONS AND ASYMMETRY IN THE ECE RADIATION TEMPERATURE

In Sec. II D, an asymmetry across the magnetic axis is predicted in the measured electron cyclotron emission due to downshifted emission from the plasma core. This asymmetry is observed experimentally and is modified by the optical depth of the plasma, which

is proportional to the plasma density. The radiation temperature measured by the ECE radiometer at approximately $r/a = 0.15$ and $r/a = 0.50$ normalized effective plasma radius on the LFS and HFS of the device is compared to Thomson scattering measurements of the electron temperature vs line-average plasma density in Fig. 8.

Emission from both the HFS and LFS of the device increases faster than the electron temperature as the plasma line-average density decreases. However, the emission measured from the LFS increases at a faster rate than that measured from the HFS of the device. Near the core of the plasma ($r/a = 0.15$), the asymmetry in the spectrum is significant below a plasma line-average density of $n_e < 3.5 \times 10^{18} \text{ m}^{-3}$. Near the half-radius, the asymmetry in the spectrum is less significant. Both measurements begin to diverge from the electron temperature for $n_e < 3.5 \times 10^{18} \text{ m}^{-3}$.

At relatively low plasma density, the condition of small disturbance, $p_{abs}/n_e T_e v_e \ll 1$, is violated in HSX as the ECRH power-per-particle becomes large. Electron cyclotron emission is sensitive to the nonthermal component of the electron distribution function, and the asymmetry across the magnetic axis in the measured ECE spectrum is enhanced by the presence of nonthermal electrons. In HSX, nonthermal electrons can also contribute significantly to the total plasma stored energy. The plasma stored energy from a diamagnetic loop is compared to the kinetic stored energy over a range of line-average densities measured using the central chord of the HSX interferometer²⁸ in Fig. 9. The launched power was held at 85 kW during this experiment. There is a discrepancy between the total plasma stored energy and the kinetic stored energy defined by the integrated profile measurements at relatively low plasma density,

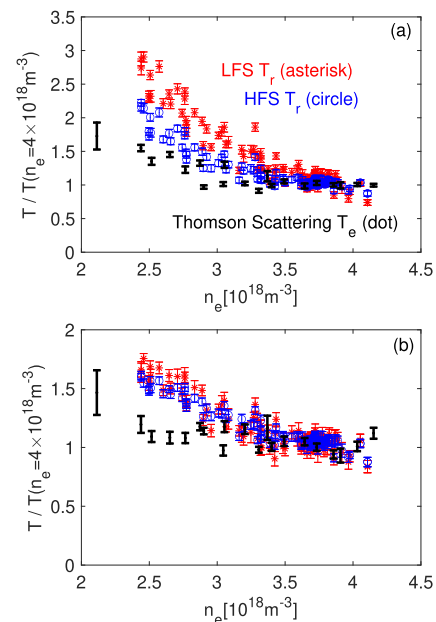


FIG. 8. Electron temperature measured by Thomson scattering is compared to radiation temperature from a LFS ECE channel (red asterisk) and a HFS ECE channel (blue circle) vs line-average density in the plasma core (a) and at the half-radius (b). Signals are normalized by their value at $n_e = 4 \times 10^{18} \text{ m}^{-3}$ to show the discrepancy in their relative behavior as plasma density decreases.

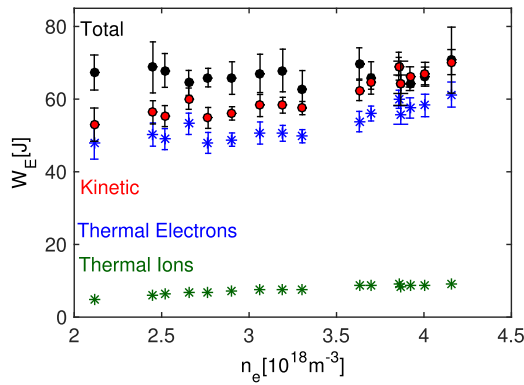


FIG. 9. Total stored energy measurement (W_E^{diam} , black circles), electron stored energy measurement ($W_{E,e}$, blue asterisks), an estimate of the energy carried by the ions ($W_{E,i}$, green asterisks), and the kinetic stored energy ($W_E^{kin} = W_{E,e} + W_{E,i}$, red circles).

and this discrepancy decreases with increasing line-average density. The ion kinetic energy is estimated from fits to charge exchange recombination spectroscopy measurements.²⁹ The two measurements converge near a line-average plasma density of $3.5 \times 10^{18} \text{ m}^{-3}$. The match in the measured diamagnetic stored energy and the kinetic stored energy is primarily attributed to increased electron thermal energy in the plasma and a decrease in the portion of the energy carried by nonthermal electrons.

A. “Bursty” behavior with high ECRH power-per-particle

Electron cyclotron emission data are not shown below a line-average plasma density of $2.5 \times 10^{18} \text{ m}^{-3}$ in Fig. 8. This is because at these plasma densities, “bursty” behavior appears in the ECE. Time-traces of the ECE signal near the core and half-radius of the plasma at a line-average density of $2 \times 10^{18} \text{ m}^{-3}$ are shown in Fig. 10. The ECE radiation temperature at the half-radius and core of the plasma is measured to spike on a fast time scale, with a peak duration of less than 0.1 ms.

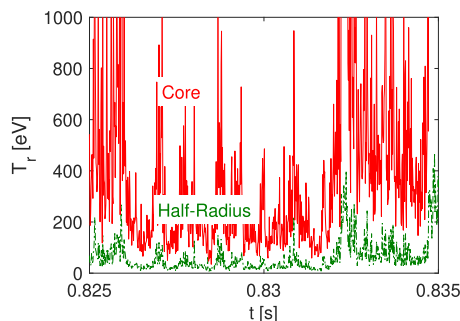


FIG. 10. “Bursty” behavior is measured in the ECE temperature in a plasma discharge with line-average density of $2 \times 10^{18} \text{ m}^{-3}$. The half-radius (green dashed-dotted, $r/a \approx 0.5$) and core (red solid line, $r/a \approx 0.15$) ECE channels.

Similar behavior was observed in the W7-AS experiment with high ECRH power densities. In W7-AS, the “bursty” phenomena were attributed to local degradation of the power absorption due to flattening of the distribution function, and the flattening of the distribution function was followed by increased absorption by collisionless-ripple-trapped electrons resonant at high energies.¹² For this reason, we take this “bursty” behavior as further evidence of the presence of nonthermal electrons at relatively low plasma density in HSX.

B. The effect of nonthermal emission on ECE localization

At sufficiently high absorbed ECRH power density, a significant nonthermal electron component may develop in HSX plasmas that alters the observed ECE spectrum. For plasmas with 85 kW launched ECRH power, Fig. 9 shows a discrepancy between diamagnetic stored energy and total kinetic energy for line-average plasma densities $n_e < 3.5 \times 10^{18} \text{ m}^{-3}$ that is attributed to nonthermal electrons. The discrepancy ($\sim 15 \text{ J}$) is the largest at the lowest plasma density ($n_e = 2.5 \times 10^{18} \text{ m}^{-3}$). To model the emission from nonthermal electrons and assess whether it may explain the deviation of the ECE spectrum from the electron temperature in Fig. 8 at relatively low plasma density, the single-pass ray tracing model of Sec. II D was repeated with a bi-Maxwellian electron distribution function. In the absence of detailed information regarding the nonthermal population, a nonthermal electron pressure profile is chosen as a Gaussian distribution confined primarily to the ECRH deposition region ($r/a < 0.2$) in this work. The nonthermal pressure profile is chosen such that the volume-integrated profile is equal to the discrepancy between plasma stored energy and total kinetic energy at $n_e = 2.5 \times 10^{18} \text{ m}^{-3}$. Based on previous experiments and modeling at HSX,^{16,26} two tail electron temperatures are considered: $T_{e1} = 5 \text{ keV}$ and $T_{e1} = 10 \text{ keV}$.

The emission shapes resulting from this bi-Maxwellian model are shown in Fig. 11 for a channel with its cold plasma resonance location near the core ($r/a = 0.15$) and near the mid-radius ($r/a = 0.5$) on both sides of the magnetic axis. For the core channels, Figs. 11(a) and 11(b), the magnitude of the emission is increased by the presence of nonthermal electrons. While the localization of both core channels is largely maintained, the LFS emission shapes extend toward the magnetic axis with increasing tail temperature. For the mid-radius channels, Figs. 11(c) and 11(d), there is a significant asymmetry in the emission shapes across the magnetic axis. The magnitude of the HFS mid-radius channel remains largely unmodified by the presence of nonthermal electrons, except where the emission shapes overlap with the nonthermal electron source, as shown in Fig. 11(c). This is not true for the LFS mid-radius channel, which is dominated by contributions from the plasma core in the presence of nonthermal electrons, as shown in Fig. 11(d). Note that even in the thermal case shown in Fig. 11, there is a significant contribution to the LFS channel by relativistically downshifted core emission.

For line-average plasma densities less than $n_e = 3.5 \times 10^{18} \text{ m}^{-3}$, the experimental behavior of the radiation temperature measured by the ECE diagnostic shown in Fig. 8 exhibits two behaviors that are well described by the single-pass bi-Maxwellian model. In Fig. 8(a), an asymmetry across the magnetic axis is measured for the core

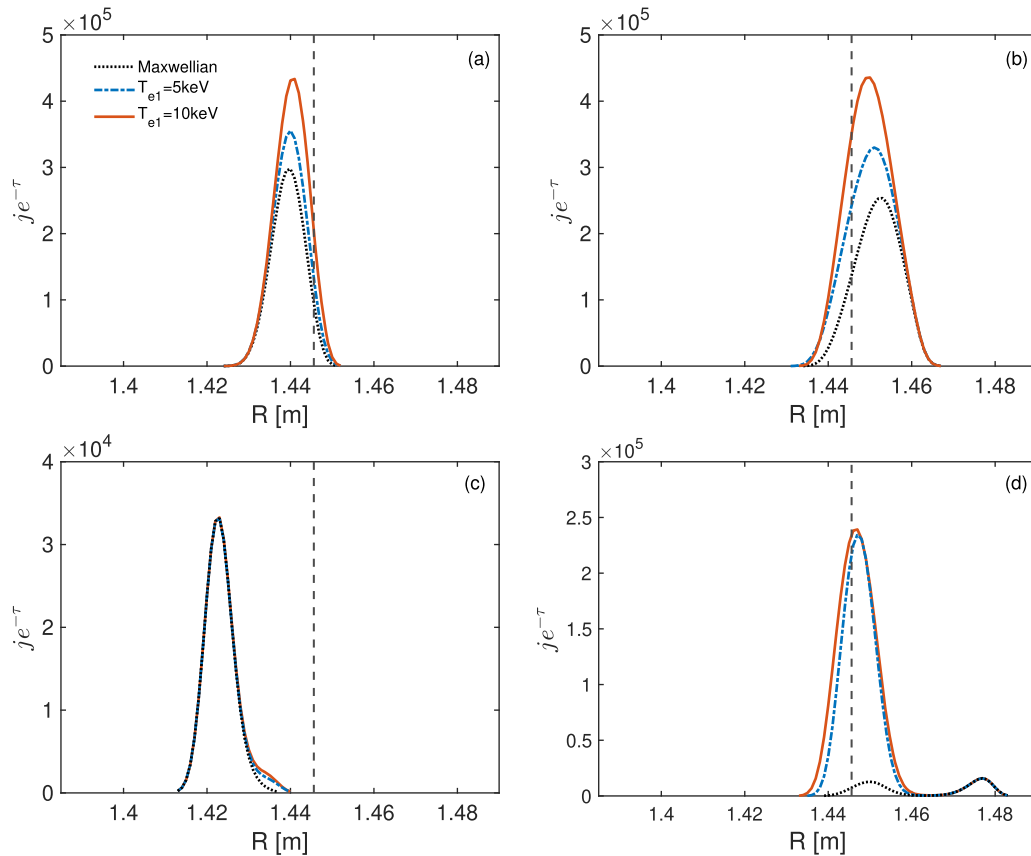


FIG. 11. Single-pass emissivity accounting for reabsorption for core channels (a) and (b) and near mid-radius channels (c) and (d) on the HFS and LFS of the magnetic axis. Results are shown for three tail populations: $T_{e1} = 0$ keV (Maxwellian, black dotted line), 5 keV (Bi-Max., blue dotted-dashed line), and 10 keV (orange solid line).

channels, and this asymmetry is measured to increase as the non-thermal electron population increases. This is reflected in Fig. 11, as the peak emission in both the HFS and LFS channels is predicted to increase in magnitude, but the increase in the integrated emission is larger for the LFS. Similarly, for the mid-radius channels, the integrated emission of the HFS channels is not predicted to change significantly, but the signal observed by the HFS channels changes in direct proportion to the nonthermal population. The LFS channels at the mid-radius have no localization in the presence of nonthermal electrons, but the signal level increases due to relativistically downshifted core nonthermal emission.

IV. CONCLUSIONS

An absolutely calibrated 16-channel heterodyne radiometer is used to measure the electron cyclotron emission on the helically symmetric experiment. At relatively low plasma density, asymmetry in the radiation temperature profile is measured, while at relatively high plasma density, the radiation temperature determined from the emission is comparable to the electron temperature measured by a Thomson scattering diagnostic. The radiation transfer has been modeled analytically as well as numerically using ray

tracing methods. Analytic modeling is used to determine the electron temperature in the core of the plasma, where the dimension of the flux surfaces is smaller than the E-plane beam width of the antenna, and an iterative procedure is used to self-consistently determine the absorption shape and resonance position of each ECE channel from the measured radiation spectrum.

A multi-pass emission model is necessary to reproduce the experimentally measured radiation temperature spectrum from the high-field side of the magnetic axis. The emission from the low-field side of the magnetic axis contains a significant portion of relativistically downshifted emission that is not reabsorbed along the line-of-sight of the diagnostic. The asymmetry in the ECE radiation temperature that is measured across the magnetic axis can be understood as originating primarily from relativistically downshifted thermal emission at a relatively high plasma density and as originating primarily from relativistically downshifted nonthermal emission at a relatively low plasma density in HSX. The energy carried by this population has been measured by comparing the integrated stored energy from kinetic profiles to that measured by a diamagnetic loop diagnostic, and the qualitative behavior of the modeled ECE spectrum is consistent with the measured ECE radiation temperatures.

ACKNOWLEDGMENTS

This work was supported by the U.S. Department of Energy Office of Science, Office of Fusion Energy Sciences, Helically Symmetric Toroidal Experiment program under Award No. DE-FG02-93ER54222. The authors would like to thank Dr. P. Aleynikov of the Max Planck Institute for Plasma Physics in Greifswald for his ongoing support of the TRAVIS ray tracing code, Professor K. Nagasaki of the Institute of Advanced Energy at Kyoto University for his guidance absolutely calibrating the radiometer, and Dr. S. Anderson and Professor D.T. Anderson of the HSX plasma laboratory for their support of the experiment.

AUTHOR DECLARATIONS

Conflict of Interest

The authors have no conflicts to disclose.

Author Contributions

G. M. Weir: Conceptualization (lead); Data curation (lead); Formal analysis (lead); Investigation (lead); Methodology (lead); Software (lead); Supervision (equal); Validation (lead); Visualization (lead); Writing – original draft (lead); Writing – review & editing (lead). **L. Singh:** Formal analysis (supporting); Investigation (supporting); Methodology (supporting); Software (supporting); Validation (supporting); Visualization (supporting); Writing – review & editing (supporting). **K. M. Likin:** Conceptualization (equal); Data curation (supporting); Investigation (supporting); Methodology (equal); Supervision (lead); Validation (equal); Writing – original draft (supporting). **N. B. Marushchenko:** Formal analysis (supporting); Methodology (supporting); Resources (supporting); Software (equal); Validation (supporting). **Y. Turkin:** Resources (supporting); Software (equal); Validation (supporting).

DATA AVAILABILITY

The data that support the findings of this study are available from the corresponding author upon reasonable request.

REFERENCES

- H. J. Hartfuss, T. Geist, and M. Hirsch, “Heterodyne methods in millimetre wave plasma diagnostics with applications to ECE, interferometry and reflectometry,” *Plasma Phys. Controlled Fusion* **39**, 1693–1769 (1997).
- S. K. Rathgeber, L. Barrera, T. Eich, R. Fischer, B. Nold, W. Suttrop *et al.*, “Estimation of edge electron temperature profiles via forward modelling of the electron cyclotron radiation transport at ASDEX upgrade,” *Plasma Phys. Controlled Fusion* **55**(2), 025004 (2012).
- T. Klinger, A. Alonso, S. Bozhrenkov, R. Burhenn, A. Dinklage, G. Fuchert *et al.*, “Performance and properties of the first plasmas of Wendelstein 7-X,” *Plasma Phys. Controlled Fusion* **59**(1), 014018 (2017).
- T. Klinger, T. Andreeva, S. Bozhrenkov, C. Brandt, R. Burhenn, B. Buttenschön *et al.*, “Overview of first Wendelstein 7-X high-performance operation,” *Nucl. Fusion* **59**(11), 112004 (2019).
- M. Hirsch, “Microwave and interferometer diagnostics prepared for first plasma operation of Wendelstein 7-X,” in *Proceedings of 1st EPS Conference on Plasma Diagnostics* (SISSA Medialab, 2016), Vol. 240, p. 111.
- M. Hirsch, U. Höfel, J. W. Oosterbeek, N. Chaudhary, J. Geiger, H. J. Hartfuss *et al.*, “ECE diagnostic for the initial operation of Wendelstein 7-X,” *EPJ Web Conf.* **203**, 03007 (2019).
- F. S. B. Anderson, A. F. Almagri, D. T. Anderson, P. G. Matthews, J. N. Talmadge, and J. L. Shohet, “The helically symmetric experiment, (HSX) goals, design and status,” *Fusion Technol.* **27**(3T), 273–277 (1995).
- A. F. Almagri, D. T. Anderson, F. S. B. Anderson, P. H. Probert, J. L. Shohet, and J. N. Talmadge, “A helically symmetric stellarator (HSX),” *IEEE Trans. Plasma Sci.* **27**(1), 114–115 (1999).
- G. M. Weir, K. M. Likin, N. B. Marushchenko, and Y. Turkin, “Ray tracing and ECRH absorption modeling in the HSX stellarator,” *Nucl. Fusion* **55**(11), 113011 (2015).
- V. Erckmann and U. Gasparino, “Electron cyclotron resonance heating and current drive in toroidal fusion plasmas,” *Plasma Phys. Controlled Fusion* **36**(12), 1869–1962 (1994).
- G. Bekefi, *Radiation Processes in Plasmas* (Wiley, New York, 1966).
- M. Romé, V. Erckmann, U. Gasparino, H. J. Hartfuß, G. Kühner, H. Maaßberg *et al.*, “Kinetic modelling of the ECRH power deposition in W7-AS,” *Plasma Phys. Controlled Fusion* **39**, 117–158 (1997).
- W. Rowan, M. Austin, J. Beno, R. Ellis, R. Feder, A. Ouroua *et al.*, “Electron cyclotron emission diagnostic for ITER,” *Rev. Sci. Instrum.* **81**(10), 10D935 (2010).
- Z. J. Yang, P. E. Phillips, G. Zhuang, J. S. Xiao, H. Huang, W. L. Rowan *et al.*, “A 16-channel heterodyne electron cyclotron emission radiometer on J-TEXT,” *Rev. Sci. Instrum.* **83**(10), 10E313 (2012).
- K. M. Likin, C. Lechte, L. Huijuan, and F. S. B. Anderson, “ECE and reflectometry on the helically symmetric experiment,” in *Proceedings of ITC/ISHW2007, Ceratopia Toki* (NIFS, Gifu, Japan, 2007), available from http://www.nifs.ac.jp/itc/itc17/file/PDF_proceedings/poster2/P2-073.pdf.
- C. B. Deng, D. L. Brower, B. N. Breizman, D. A. Spong, A. F. Almagri, D. T. Anderson *et al.*, “Energetic-electron-driven instability in the helically symmetric experiment,” *Phys. Rev. Lett.* **103**(2), 025003 (2009).
- S. Murakami, U. Gasparino, H. Idei, S. Kubo, H. Maassberg, N. Marushchenko *et al.*, “5-D simulation study of suprathermal electron transport in non-axisymmetric plasmas,” *Nucl. Fusion* **40**(3Y), 693 (2000).
- Y. Yamamoto, S. Murakami, C. C. Chang, S. T. A. Kumar, J. N. Talmadge, K. M. Likin *et al.*, “Parallel flow driven by electron cyclotron heating in the helically symmetric experiment,” *Nucl. Fusion* **62**(6), 064004 (2022).
- K. Zhai, F. S. B. Anderson, K. Willis, K. Likin, and D. T. Anderson, “Performance of the Thomson scattering diagnostic on helical symmetry experiment,” *Rev. Sci. Instrum.* **75**(10), 3900–3902 (2004).
- S. P. Hirshman and J. C. Whitson, “Steepest-descent moment method for three-dimensional magnetohydrodynamic equilibria,” *Phys. Fluids* **26**(12), 3553–3568 (1983).
- A. G. Litvak, *High-Frequency Plasma Heating* (American Institute of Physics, 1992), p. 13, Eq. 28.
- N. B. Marushchenko, V. Erckmann, H. J. Hartfuss, M. Hirsch, H. P. Laqua, H. Maassberg *et al.*, “Ray tracing simulations of ECR heating and ECE diagnostic at W7-X stellarator,” *Plasma Fusion Res.* **2**, S1129 (2007).
- N. B. Marushchenko, Y. Turkin, and H. Maassberg, “Ray-tracing code TRAVIS for ECR heating, EC current drive and ECE diagnostic,” *Comput. Phys. Commun.* **185**(1), 165–176 (2014).
- P. F. Goldsmith, “Quasi-optical techniques,” *Proc. IEEE* **80**(11), 1729–1747 (1992).
- K. M. Likin, J. N. Talmadge, A. F. Almagri, D. T. Anderson, F. S. Anderson, C. Deng *et al.*, “Absorption of x-wave at the second harmonic in HSX,” *AIP Conf. Proc.* **694**(1), 331–334 (2003).
- K. M. Likin, A. Abdou, A. F. Almagri, D. T. Anderson, F. S. B. Anderson, D. Brower *et al.*, “Comparison of electron cyclotron heating results in the

helically symmetric experiment with and without quasi-symmetry," *Plasma Phys. Controlled Fusion* **45**(12A), A133–A142 (2003).

²⁷G. M. Weir, B. J. Faber, K. M. Likin, J. N. Talmadge, D. T. Anderson, and F. S. B. Anderson, "Profile stiffness measurements in the helically Symmetric experiment and comparison to nonlinear gyrokinetic calculations," *Phys. Plasmas* **22**(5), 056107 (2015).

²⁸C. Deng, D. L. Brower, W. X. Ding, A. F. Almagri, D. T. Anderson, F. S. B. Anderson *et al.*, "First results from the multichannel interferometer system on HSX," *Rev. Sci. Instrum.* **74**(3), 1625 (2003).

²⁹A. Briesemeister, K. Zhai, D. T. Anderson, F. S. B. Anderson, J. Lore, and J. N. Talmadge, "Flow velocity measurements using CHERS in the HSX stellarator," *Contrib. Plasma Phys.* **50**(8), 741–744 (2010).